BioSaFe: Bioprinting Security Framework for Detecting Sabotage Attacks on Printability and Cell Viability

Muhammad Ahsan*, Eunice Pak†, Kate Jackson †, Muhammad Haris Rais‡, Barry Najarro-Blancas
†, Nastassja Lewinski †, Irfan Ahmed*,
*Department of Computer Science
†Department of Chemical and Life Science
Virginia Commonwealth University (VCU), Richmond, USA
‡Department of Computer Science
Virginia State University (VSU), Petersburg, USA
Email: {ahsanm5,nalewinski,iahmed3}@vcu.edu

Abstract—Additive manufacturing (aka, 3D printing) is increasingly used in bioprinting to create objects layer by layer from ground zero. As research and development progress in bioprinting technology for medical applications, ensuring the security of 3D bioprinters against adversarial attempts becomes critical. This paper proposes six novel sabotage attacks on two types of bioprint constructs as case studies, i.e., a multilayered square box and a human ear, to show that attackers can deliberately manipulate the bioprinting process to sabotage a bioprinted construct. We use quality assurance metrics, i.e., printability and cell viability, to demonstrate the impact of these attacks on the printed constructs. Furthermore, this paper introduces BioSaFe, a bioprinting security framework for real-time monitoring of critical printing parameters per-layer basis, including nozzle temperature, layer thickness, UV curing, HEPA filter status, print geometry, and print speed. BioSaFe employs spatiotemporal modeling and interpolation functions to compare in-situ sensing data with a reference G-code file (being used for printing) in both space and time domains. This direct comparison does not require a training phase on printed objects and enables BioSaFe to start monitoring from the first printing job, supporting Industry 4.0 for mass customization. Our evaluation results show that BioSaFe can accurately detect our sabotage attacks, demonstrating its potential in safeguarding bioprinting processes.

Index Terms—Additive Manufacturing, Bioprinting, in-situ monitoring, Sabotage, Cyber Security

I. INTRODUCTION

Bioprinting, an additive manufacturing (AM) application, allows precise layer-by-layer deposition of biomaterials to form complex 3D structures [1]. As of 2023, the global market size of 3D bioprinting is projected to increase from USD 1.6 to 6.9 billion by 2032 with an annual growth rate of approximately 16% [2]. In particular, bioprinters are increasingly utilized in tissue engineering to addressing organ shortages and transforming medical treatments; they create tissues and organs for transplantation [3], [4] and regenerative medicine [5]. Bioprinting's pivotal role extends to drug testing, where bioprinted constructs serve as realistic tissue and disease models. These models have been instrumental in studying terminal illnesses like cancer [6] and infectious diseases like SARS-CoV-2 (COVID-19) virus for vaccine development [7].

Extrusion-based bioprinting (EBB) is one of the most common and economical bioprinting techniques [8]. It uses pressure pistons or a reciprocating screw, with pneumatically controlled extrusion being more common and cost-effective. The EBB process involves the precise extrusion of biomaterial through a temperature and pressure-controlled nozzle. The nozzle moves in two dimensions (x and y), while the print bed moves along the z-axis, providing complete 3D control.

Multiple printing parameters are set and controlled before and during bioprinting to achieve the final print geometry [9]. They include temperature, extrusion pressure, print speed, nozzle diameter, layer thickness, and cross-linking, and must be optimized to ensure the structural integrity of a printed construct. Adversaries manipulate these parameters slightly to cause nonconformity with the design specifications. They are called sabotage attacks [10], [11], where the goal is to weaken, damage, or destroy the construct.

This paper proposes six novel sabotage attacks targeting different parameters of the bioprinting process. The attacks include; nozzle switching to alter print composition by switching materials, ultraviolet (UV) curing targeting the post-processing gelation process, thermodynamic manipulation targeting cell viability, a quick pause in printing to compromise structural integrity by introducing micro-defects, and contamination targeting the filtration unit.We demonstrate and evaluate the attacks on two case studies: a multilayer print construct and a bioprinted human ear construct. We use quality assurance metrics, i.e., printability and cell viability, to evaluate the attacks' impact on the constructs [8].

This paper further proposes BioSaFe, a defensive framework against sabotage attacks on bioprinters. BioSaFe collects and analyzes in-situ sensor data to identify sabotage attempts in printing. It employs spatiotemporal modeling and interpolation functions to align G-code and sensing data into comparable space and time domains. This comparison does not require a prior learning phase, allowing BioSaFe to start monitoring from the first printing job, which aligns with Industry 4.0 for mass customization. BioSaFe framework leverages layer changes as logical indicators to divide the 3D geometry into 2D layers. By validating multiple printing parameters, such as per-layer geometry, layer thickness, timing profile, thermal profile, HEPA (High-Efficiency Particulate Absorbing) filter

fan profile, and UV profile, BioSaFe ensures the integrity of the printing process. This per-layer data analysis identifies attacks at the precise layer, thereby saving production time and minimizing material wastage. We evaluate BioSaFe on our sabotage attacks using the Cellink bioprinter. Our evaluation shows that BioSaFe can detect these attacks accurately.

The contributions of this work can be summarized as follows:

- We study the sabotage attacks pertinent to the bioprinting process and their adverse effects on cell viability and the printability of printed constructs.
- We create a security framework, BioSaFe, for safeguarding bioprinters against sabotage attacks. BioSaFe is designed to support Industry 4.0 for mass customization, not requiring a prior learning phase. Thus, it can start monitoring from the first printing job, irrespective of print geometry.
- We evaluate the BioSaFe framework against our sabotage attacks, demonstrating its effectiveness in monitoring critical printing parameters.
- We evaluated the attacks and framework implementation on the Cellink INKREDIBLE+ 3D bioprinter, a commonly used printer in real-world applications.

II. RELATED WORK

Most techniques in the literature are tuned to a particular print geometry, making them ill-suited for mass customization and adaptable to changing printing needs. Moreover, bioprinting, which employs bioink to create constructs, involves distinct printing parameters and settings, presenting unique monitoring challenges. The proposed framework, BioSaFe, addresses this gap by offering accurate and minimally intrusive process monitoring adaptable to application needs. The rest of the section offers insights into bioprinting quality assurance research and reviews state-of-the-art AM monitoring techniques.

A. Bioprinting Quality Assurance

Bioprinting, a relatively newer application in the field of AM, holds promise for applications in tissue engineering and regenerative medicine due to its ability to create intricate 3D tissue structures. Researchers are actively studying the impact of alterations in printing parameters on the final printed constructs, such as improving resolution for micron and submicron features [12]. For example, the standoff distance, typically recommended to be the nozzle's inner diameter or around 80% of that height, affects filament width and can result in smearing, stretching, or breakage [13]. Similarly, temperature settings can also impact physical features and cell behavior. For example, the A549 lung cancer cell proliferates best at internal body temperature ($\sim 37^\circ C$), but at hyperthermia conditions (42–$48^\circ C$ for 30–120 min) results in genotoxicity and cytotoxicity [14].

Unlike temperature settings, UV light does not significantly impact the printability of the final constructs when using non-crosslinkable material; however, it can affect cell viability.

Metho-dology	Ref.	Mate-rial	Per obj. Profile	Side channel	SC Limitation			Monitored Process				Attack Stealth
					Sen.	Int.	CC	Kin.	Thrm.	UV	Fltr	
Product Verif.	[20]	Poly	✓	X-ray CT	○	○	●	✓				●
	[21]	Poly	✓	Acoustic	●	○	●	✓				○
	[22]	Metal	✓	X-ray CT	○	○	●	✓				●
In-situ Print Verif.	[23]	Poly	✓	Acoustic	●	○	●	✓				●
	[24]	Poly	✓	Acoustic	●	○	●	✓				◐
	[25]	Poly	✓	Elect. Current	○	●	●	✓				●
	[26], [27]	Poly	✓	Opt. Camera	◐	●	◐	✓				○
	[28], [29]	Poly	✓	Opt. Camera	●	●	◐	✓				○
	[30]	Poly	✗	Multiple Sens.	◐	●	◐	✓				○
	[31]	Poly	✗	Multiple Sens.	○	◐	○	✓	✓			●
	[32]	Metal	✓	IR Camera	●	○	●		✓			◐
	[33]	Metal	✓	Ultrasonic	●	○	●	✓				●
	BioSaFe	Bioink	✗	Multiple Sens.	○	●	○	✓	✓	✓	✓	●

* Sen.: Sensitivity, Int.: Intrusitivity, CC: Caliberation Complexity
* Kin.: Kinetic, Thrm,: Thermal, ●: High, ◐: Medium, ○: Low

TABLE I: Comparison of monitoring techniques in additive manufacturing; last row is our proposed BioSafe framework.

Shorrocks et al. [15] studied the effect of UVA on immortalized human keratinocytes derived from the skin (HaCaT cells). The study reveals shorter UV dosage rates led to higher cytotoxicity and genotoxicity even when receiving the same total UVA dose (with peak spectral irradiance output at 365 nm). However, the data may not accurately represent the lesser researched effects of UV exposure on internal organ cells, such as the A549 cell line, derived from human lung alveolar epithelial cells, used in the current study.

Cell viability and printability ratio (Pr), unique metrics in 3D bioprinting, have been proposed as key criteria for evaluating printability [8] and assessing post-printing pore shape fidelity [16], respectively. While there are several proposed quality assurance metrics for bioink printability, due to the novelty and case-by-case specificity of each bioink formula, there are currently no official standards set in place. Guidelines for physical scaffold and cell viability, such as good cell and tissue culture practice [17], exist. However, to date, there are no specific regulatory requirements for bioprinting [18], [19]. These endpoints help set a measurable standard for what qualifies as a good versus bad print and characterize the effects of the bioprinter's settings on the final construct.

B. AM Process Monitoring Techniques

Table I presents an overview of the current literature for securing the AM process. Based on the methodology, current techniques can be classified into either offline verification, where a completed print is subjected to non-destructive testing to verify its integrity [20], [21], or real-time in-situ process verification [23], [24], [30]. Researchers have investigated multiple side channels for real-time monitoring of the printing process. However, due to its intrinsic nature, each side channel is limited by multiple factors, including sensitivity, intrusiveness, and calibration complexity [11]. Acoustic data [21], [23], [24] provides kinetic process information, including nozzle and print bed moves; however, it is subject to high noise sensitivity. Similarly, electric current [25], while more resistant to noise depending on usage, could be highly intrusive.

The majority of side-channel research has focused on monitoring kinetic printing parameters, but thermal process manipulation is also a potential threat [34]. Thermal sensors on the nozzle and print bed provide real-time data for process authentication but cannot capture kinetic data. To address this, researchers have suggested using multiple sensors [31], [30] to
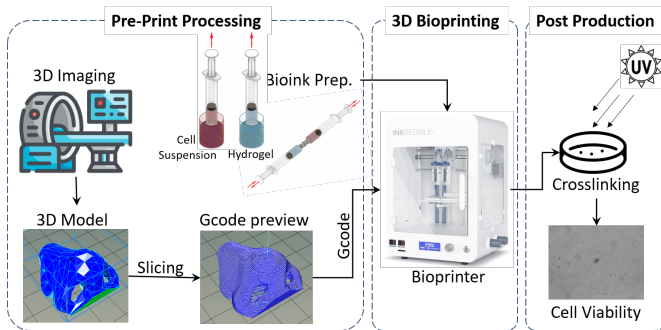
Fig. 1: Extrusion Bioprinting process chain.

Ref.	Material Type	Printing Parameters of Sabotage Attacks								
		NS	OG	Th	LT	FK	IF	PS	UV	FS
[25]	Polymer		✓		✓	✓	✓	✓		
[34]				✓		✓				
[31]			✓	✓	✓	✓	✓	✓		
[30]					✓		✓	✓		✓
[20]		✓	✓		✓	✓	✓			
[22]	Metal					✓				
[32]						✓				
this paper	Bioink	✓	✓	✓	✓	✓	✓	✓	✓	✓

* NS: Nozzle State, OG: Outer Geometry, Th: Thermal, FS: Fan Speed
LT: Layer Thickness, FK: Filament kinetics, IF: Infill, PS: Print Speed

TABLE II: Comparative survey of sabotage attacks.

collect comprehensive process information, including kinetics, thermal dynamics, and fan speed.

Depending on the specific application, the printing parameters can significantly vary, necessitating different sensing techniques for effective monitoring. Consequently, the techniques established for monitoring polymer-based AM processes might not apply to metal or bio AM processes. While there has been research available on securing 3D printed polymer implants [20], [21], no such study is available for bioprinted constructs.

III. BIOPRINTER SABOTAGE ATTACKS

The sabotage attacks in the literature on 3D printers have been examined in the context of polymer and metal materials. They are different for bioink in this paper, as presented in Table II. Nonetheless, due to the distinct process chain, printing parameters, and quality assurance criteria in bioprinting, the adversarial consequences of these attacks differ and are detailed in this section.

A. Bioprinting Process Chain

There are 3 stages associated with the EBB process chain, including i) pre-print preparation, ii) the printing stage, and iii) the post-print phase, as shown in Figure 1. The first stage involves collecting the 3D geometry information of the part to print by using any of the imaging techniques, including MRI, CT Scan, ultrasound, etc. The images are then fed into computer-aided design (CAD) software, which renders the model to stereolithography (STL) file format, representing the 3D geometry as a set of conjunctional triangular shapes. Provided with the printing parameters, the slicing software then converts the file to a set of machine instructions (G-code). As a part of the pre-print setup, bioink-containing cells and hydrogel suspension are also prepared to be used for printing.

The second phase is the actual printing process, where the G-code instructions are communicated to the printer, typically through a USB or ethernet connection. The firmware in the printer interprets these instructions and controls motors and actuators accordingly. Once printing is completed, the print is cured using UV radiation to achieve gelation. Subsequently, quality tests, such as printability and cell viability, are performed to ensure conformance to the design.

B. Quality Metrics

1) Cell Viability: Cell viability [8] refers to the percentage of cells that remain alive after printing. Directly after printing, cells are stained with NucBlue Live Cell Stain (which stains all cells) and propidium iodide (which stains only dead cells). The cells are photographed at several different locations using a fluorescence microscope and analyzed for cell counts at fixed thresholds and camera gain settings. Cell viability is considered optimal at a threshold above 90% average from after cell harvest.

2) Printability Ratio: The printability ratio (Pr) [8] is a dimensionless method of defining bioink printability. Mathematically it is defined as $Pr = L^2/16A$, where 'L' refers to the perimeter of a given cross-sectional area at the base of the pore and 'A' refers to its cross-sectional area. It is altered from the circularity formula, where a Pr value of < 1 indicates a smaller degree of gelation, and a $Pr > 1$ indicates a larger degree of gelation. A Pr of exactly 1 indicates a perfect square shape formed by the gel. The further the Pr value is from 1, the lower the shape fidelity and printability.

C. Adversarial Model and Assumptions

In a multilayered smart bioprinting ecosystem, there are multiple components involved in the process chain, each potentially susceptible to manipulation and exploitation by the attacker [35]. For instance, vulnerabilities have been identified in firmware [36], [37], [38], slicer software [39], communication protocols [40], [41], control PC systems [42], and other crucial elements. These vulnerabilities present avenues through which the adversary could achieve their malicious intentions [43], [44]. By leveraging weaknesses in these components, the attacker can manipulate printing parameters and disrupt the bioprinting process, thereby achieving their goal of sabotaging the final print construct.

Adversarial Capabilities. The attacker exhibits capabilities to manipulate printing parameters, enabling them to introduce malicious alterations either through G-code files, CAD files, slicing parameters, or firmware configurations. For example, the adversary can enact changes to the printing process by adding, removing, or modifying commands within the G-code file. This manipulation can occur through various means, including direct manipulation of the slicer software process memory, as evidenced by Kurkowski et al. [39], hijacking unencrypted communication channels, as presented by Rais

et al. [10], or through the injection of malware into the printer firmware, as demonstrated by Pearce et al. [38].

Attacker Motivation. Bioprinters with their wide range of potential applications, make them a lucrative target for adversaries. For instance, altering bioprinting parameters or the digital blueprints of medical implants can result in defective products, leading to failed surgeries or severe patient harm. Such incidents can erode public trust in bioprinting technologies and expose companies to substantial legal liabilities and financial losses. The proposed attacks demonstrate the adversarial objectives that can be achieved through subtle manipulations of printing parameters. BioSaFe ensures the integrity of these parameters from malicious tampering through real-time monitoring.

Defender Capabilities. We assume that the defender has access to the ground truth G-code file. The G-code file, verified and downloaded from a secure, authenticated server, provides a baseline for comparison. Furthermore, the monitoring system is isolated from the printing process through air-gapped measures, ensuring that potential compromises in the printing environment do not directly impact the detection and response capabilities. While air-gapping significantly reduces the risk of compromising the monitoring system [25], it requires strict access-control policies and restricted physical access to mitigate insider threats. Additionally, the monitoring sensors are protected against adversarial manipulations by maintaining measures to prevent injection attacks [45].

BioSaFe enhances existing network defense measures by detecting sabotage attacks, including those arising from supply-chain vulnerabilities targeting printer firmware. Insider sabotage threats, such as those exemplified by the Stuxnet attack [46], can also be effectively monitored through in-situ process monitoring.

D. Sabotage Attacks

In the EBB process, multiple parameters are involved, which are set/controlled before/during the printing process. Any adverse changes to them could potentially change the part's conformance to expected design behavior. Therefore, sabotage attack [11] refers to any process anomaly aimed at deterring the part's quality to render it useless or fail during operation. Figure 2 shows the studied attacks, in the context of bioprinting and are detailed below.

1) Nozzle Switching Attack: Certain experiments and biomedical applications require the use of more than one cell type in a single culture, also known as co-cultures. These different cell types may require different conditions to survive, proliferate, and reflect *in vivo* metabolic activity and cell-to-cell interactions. Specifically, cell-to-cell interactions in co-culture systems highly depend on their extracellular environment [47]. By embedding cells within a hydrogel and creating a bioink, complex cell patterns, levels of contact or separation, and diffusion between cells can be controlled.

Without specifically dyeing each bioink a distinct color and assuming both bioinks are of similar structural integrity, it is likely impossible to tell where each bioink was used in
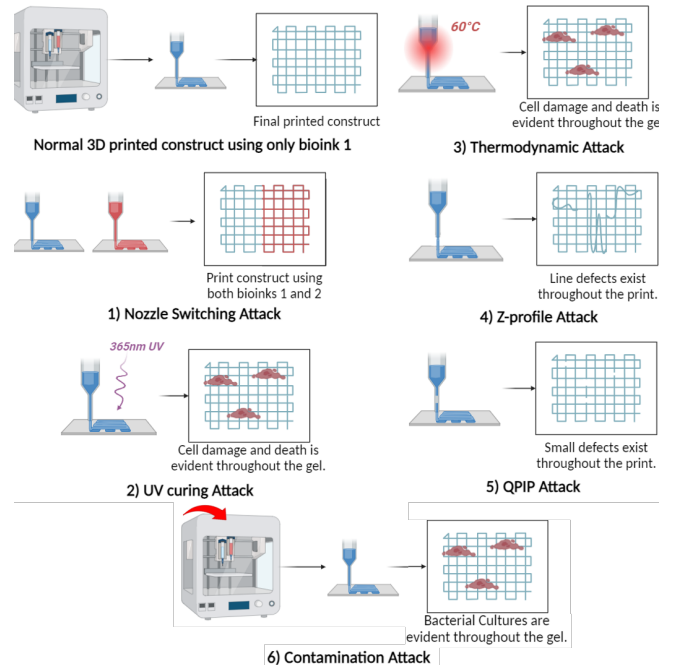

Fig. 2: Sabotage attacks on EBB Bioprinter.

the construct from sight alone. The locations of two different cell types from these cartridges within the gel would be indistinguishable. An adversary could, therefore, leverage this and attempt to sabotage the construct by switching between different nozzles while introducing minimal footprint to the final built geometry.

2) UV Curing Attack: Many bioinks require UV light curing for crosslinking and hardening. The dosage of UV radiation (mJ/cm^2) can be calculated by multiplying the UV radiation intensity (mW/cm^2) by the exposure duration in seconds. An adversary may attempt to manipulate the exposure time or the wavelength required for UV curing, leading to modification in the delivered UV dose. Overexposure to UVA and UVB light can produce harmful photo-products that can damage DNA and introduce harmful mutations that are the underlying cause of many diseases, including cancer [48]. For instance, in a study by Klak et al. [49], various cell types were exposed to UV light in Petri dishes. Their findings indicate that 5 mins of continuous exposure to 365nm UV light provides a dose of 3,381 mJ/cm^2, which is not suitable for live cells, as it leads to significant DNA damage over time across all cell types. On the other hand, an attack leading to underexposure to UV light prevents the photochemical reaction necessary for hardening the bioink polymer resulting in a geometrically unstable print construct.

3) Thermodynamic Attack: Temperature is a critical factor in the bioprinting process as it profoundly affects the gelling of the hydrogel, leading to variations in the behavior of bioink extrusion [50]. Temperature also affects cell viability [51], making it essential to optimize temperature settings to achieve the highest possible cell viability. Any adversarial manipulation of temperature settings could compromise the

4

structural integrity and cell viability.

4) Z-Profile Attack: The distance between the nozzle and the print bed, also known as the standoff distance, is a critical factor that influences the printability of the construct [52]. Specifically, a higher nozzle distance can lead to challenges in generating sharp corners due to the delay in filament response to changes in the nozzle direction [53]. An attacker intentionally modifying the layer height could potentially lead to printing defects and, hence, compromised structural integrity.

5) Quick Pause in Print (QPIP): Quick Pause in Print refers to the quick stopping and starting of pneumatic extrusion pressure on the cartridge piston. An adversary could employ this technique to subtly compromise a print, leading to the creation of gaps and bubbles when the nozzle momentarily stops extruding. This can ultimately degrade the structural integrity of the printed object.

6) Contamination Attack: The printer employs clean chamber technology to maintain a microbial-free printing environment. However, attacking the filtration system compromises air purification, thereby potentially contaminating the final print construct [54].

IV. PROPOSED SECURITY FRAMEWORK

The proposed framework (BioSaFe) for the detection of sabotage attacks on EBB is shown in Figure 3. The framework consists of multiple modules working in conjunction to ascertain the EBB process integrity. BioSaFe uses sensors to collect process information coming from the printing environment. The data is evaluated using G-code as a source of truth. Both sensing data and G-code are converted to comparable space and time domains. This allows BioSaFe to evaluate new print geometry data without needing to learn a master signature for comparison, making it well-suited to work automatically with customized geometries. BioSaFe consists of four modules where data from each module is used as input for the next module, for further processing and analysis.

A. Data Acquisition

The data acquisition module involves sensors that capture vital printing process information. It includes kinetic data such as nozzle (x/y dimensions), bed (z-dimension), and extrusion kinetics. Thermal data is gathered by measuring the nozzle temperature. The curing profile data monitors UV source timing and intensity. Additionally, the HEPA filter status is tracked through fan speed.

The data acquisition module operates independently from the printing process, acquiring all sensing information. The collected data is then transmitted serially to the PC for further processing. The acquisition module periodically records the sensing information and sends the time-stamped data to the transformation module. Considering EBB technology the details on acquiring these parameters are provided as follows.

Nozzle/Bed Kinetics Acquisition. The printer employs linear motor actuators that are coupled with corresponding axes using belts, shafts, and gears. The motors provide mobility to the printhead/nozzle in the x and y planes and print-bed in
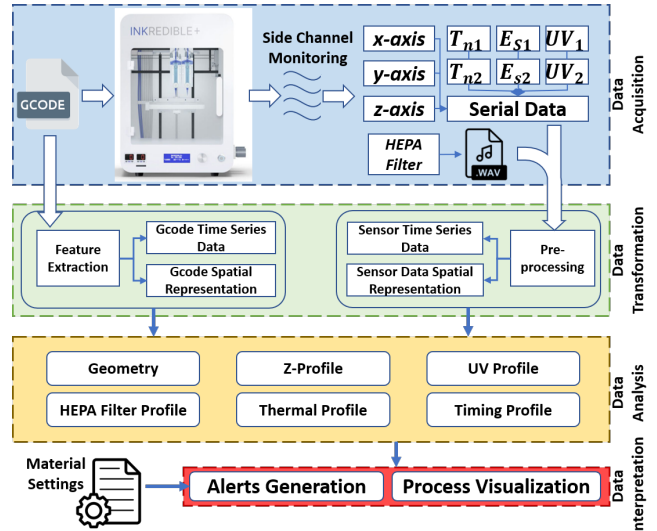

Fig. 3: Proposed (BioSaFe) Security Framework.

the z plane thereby providing complete 3D mobility. Various sensors can be deployed for independent data collection to provide real-time, precise location information of the nozzle and print bed. However, sensors, such as acoustic, vibration, or current-based sensors, either lack the required accuracy or are highly intrusive, which can disrupt the physical printing process. Similarly, the optical camera's monitoring view is often obstructed by the printer nozzle, limiting its ability to effectively capture the print geometry. To address this, optical rotary encoders coupled to the shafts of the stepper motors are chosen. The encoders translate the rotary motion to linear displacement allowing for accurate nozzle and bed position tracking.

Extrusion Data Acquisition. With most of the EBB printers, the pressure in the system is adjusted and controlled manually through an external physical knob and is therefore not monitored by the framework. However, the extrusion process is initiated using G-code commands, which activate solenoid valves that, in turn, actuate the nozzle extrusion. The extrusion itself is managed through two separate sequences: the first sequence puts the nozzle in the active position, while the second sequence triggers the actual extrusion through the nozzle. Therefore, the framework captures the signals to those actuating valves to monitor the extruder state.

Temperature Data Acquisition. The extrusion process does not necessitate heating the cartridges as a standard requirement. Nevertheless, in specific applications, it may be necessary to heat or maintain specific temperatures for the bioink material used in printing. To address this, some printers offer specialized temperature control capabilities through the metallic cartridge holder. This holder ensures that the cartridge containing the bioink is in direct contact with the metallic surface, enabling the conduction process to heat the ink. The firmware, running on the printer's board, then maintains the desired temperature throughout the printing process. To independently monitor the temperature of each nozzle, BioSaFe

employs surface-mount thermistors attached to cartridge heating elements, enabling temperature capture and monitoring.

UV Data Acquisition. Some EBB printers facilitate post-processing by turning on UV light. After printing, the construct may undergo UV curing to promote the gelation of photo-crosslinkable polymers. Depending on the material type and construct shape the curing time varies. Curing is initiated by sending a G-code command, which actuates the UV for the specified period. To measure the UV dosage, the framework incorporates a UV sensor, allowing it to determine the type of UV source being used and the duration for which it is turned on. Additionally, to measure the distance between the print bed and the UV source, the framework utilizes the z-axis sensor measurements.

HEPA Filter Status Acquisition. The EBB printers equipped with the filtration unit have a fan attached to it that controls the airflow within the chamber, and its speed is regulated through G-code commands. The fan operation generates sound, which can help estimate the fan's status and speed. To leverage this information, the framework includes a microphone near the filtration unit, which captures the noise data for further analysis. The captured data is stored in an audio (.wav) format, enabling subsequent processing and analysis. The captured data is transformed into the frequency domain, where fan-related frequencies are isolated. These frequencies are then filtered and analyzed to minimize the impact of surrounding noise, ensuring more accurate detection of fan speed.

The captured sensing data and G-code are transformed and represented in the space and time domains to facilitate comprehensive data analysis and comparison. This transformation enables coherent representation, ensuring compatibility between the two datasets. The mathematical representation for each domain is detailed in Appendix A with the transformation presented in the next section.

B. Data Transformation Module

The captured sensing data from the acquisition phase, along with the G-code file, are then transmitted to the data transformation module. Both datasets undergo transformation functions to convert them into more interpretable space and time domains.

1) G-code Transformation: G-code serves as a set of instructions that can be read by machines to configure various parameters, such as print speed, acceleration, nozzle temperature, fan speed, and UV curing settings. Additionally, the G-code includes move commands that control the nozzle position in the x and y axes, layer height in the z-axis, as well as extrusion activity during the printing process.

Converting G-code move commands into a time-series representation necessitates motion equations, as these commands only offer endpoint information. These equations factor in maximum speed and acceleration constraints to establish nozzle position between these endpoints at any point in time. Algorithm 1 (Appendix B) is used to convert G-code move commands into time-series data. The printer firmware, based

on the maximum acceleration and distance traveled, employs a triangular or trapezoidal speed profile to control the acceleration and deceleration of the print head. The algorithm, given coordinates; initial (NP_{x1}, NP_{y1}), final (NP_{x2}, NP_{y2}) along with maximum speed v_{max} and acceleration (a_{max}), returns the nozzle position at each time interval (Δt) with timestamps. The algorithm only details steps for the triangular motion profile. For the trapezoidal motion, similar steps are followed to calculate the nozzle position during the acceleration, constant speed, and deceleration phases of the motion.

Algorithm 2 (Appendix B) converts G-code into a space domain representation. It uses the G-code move instructions to extract the coordinates and the status of the extruder. Depending on whether nozzle 1 or 2 is activated, the algorithm plots the line in black or blue, respectively. For G-code move commands with no extrusion, red color lines are added. The algorithm identifies the layer change event (LC_i) as a marker to finalize the current layer plot, which is then stored with the name *"plot_{layerNum}.png"*. Subsequently, the algorithm proceeds to create and plot a new layer. This process continues until all the layers have been plotted and saved.

2) Sensing Data Transformation: The sensing data is originally recorded in a format where each entry is sampled at regular intervals (Δt). However, to estimate the fan speed, the sampled audio file needs to be transformed from the time to the frequency domain, and then interpolation is used to estimate speed. Equation 1 represents the fan speed profile during the complete printing process.

$$FSP = [(t_1, FS_1), (t_2, FS_2), ..., (t_n, FS_n)] \qquad (1)$$

To create a spatial representation of the print geometry, the same algorithm (Algorithm 2) employed for converting G-code is utilized. The algorithm takes serial data points, including nozzle positions, as input for plotting. The figure is saved and closed when a change in the z-axis value exceeding a predefined threshold is detected.

C. Data Analysis for Integrity Check

By transforming both G-code and serial sensing data into a more comparable and standardized format, the task of correlating and comparing the data becomes significantly more convenient. This allows for a more effective analysis of the printing process, enabling insights between the expected behavior (G-code) and the actual behavior (sensing data) of the 3D printer. Using the transformed data, the process verification is further detailed below.

1) Geometry Verification: The framework incorporates per-layer geometry verification, encompassing both the infill and outer structure when detecting variations. To achieve this, the sensor data and G-code spatial domain representations undergo image processing techniques to capture variations. The resultant difference image helps identify variations in the print geometry.

2) Z-Profile Verification: The Z-profile records all the layer changes during the printing process. Each time the z-axis engages and a change greater than the specified threshold is

detected, the corresponding z-axis value is added to the layer change event array (LC). The LC vector from G-code and sensing data is recorded and compared to validate the layer thickness enabling the framework to verify the consistency and accuracy of the thickness profile throughout printing.

3) Timing Profile Verification: The framework employs two vectors to verify the timing profile: TP_{G-code} and TP_{sensor}. The timing profile for the G-code is derived from the transformation function and is synchronized with the sensing data, enabling a direct comparison between the two. By comparing these vectors, the framework can detect variations in printing speed. Such variations could result in under or over-extrusion in the printed construct, without significantly changing the print geometry. The timing profile could also help identify other anomalies, e.g. thermal and UV curing attacks, where the attack changes the original print time. The framework maintains the timing profile per-layer basis, allowing for the detection of specific layers affected by the malicious changes.

4) Thermal Profile Verification: For thermal profile verification, the sensor temperature reading is compared against the G-code data. The G-code selects and sets the corresponding nozzle temperature by sending in control instructions. The framework maintains the temperature profile during the printing which is then compared against G-code to validate any malicious temperature changes.

5) UV Profile Verification: To verify the UV curing profile, the framework considers three main factors: the distance from the source (z_k), the duration for which the UV light is turned on (TD_k), and the type of UV light (UV_i). These factors are utilized to create the UV curing profile, represented mathematically as

$$UVP = [(TD_1, UV_i, z_1), (TD_2, UV_i, z_2), ..., (TD_n, UV_i, z_n)] \tag{2}$$

The captured UV curing profile is then compared with the G-code-generated profile. This ensures that there is no discrepancy in the curing process and that the correct UV source, distance, and time duration are used.

6) Fan Speed Profile Verification: After data transformation, the estimated fan speed (FS) is recorded at regular intervals, generating a profile mathematically defined by equation 1. This recorded speed profile is then compared with the fan speed specified in the G-code. By conducting this comparison, the framework verifies that the fan speed remains consistent with the G-code instructions.

V. IMPLEMENTATION

The sabotage attacks and the proposed BioSaFe framework were evaluated through their implementation on the CELLINK INKREDIBLE+ [55] 3D bioprinter. The bioprinter is equipped with a dual printhead, allowing for simultaneous printing with multiple materials or configurations. It also provides temperature control, enabling regulation of the nozzle temperature to ensure optimal printing conditions for different bioinks. Furthermore, the printer also features dual wavelength UV curing (365nm and 405nm). The printer is also equipped with

a HEPA filter-controlled printing chamber. This filtration unit employs an H14 HEPA filter along with a pre-filter, effectively removing unwanted organisms with an impressive retention rate of 99.995% [55].

To demonstrate the effects of the sabotage attacks, we used multilayered square and ear-shaped prints. The square-shaped print allows for a clear assessment of the hydrogel's smoothness, homogeneity, and swelling. The ear print helps demonstrate the effect of these attacks on constructs in real-life medical applications. Bioink preparation steps used for printing are detailed in Appendix C.

A. Attacks Implementation

The attacks were implemented by altering the G-code file, assuming that an adversary gains unauthorized access to it and can manipulate it as detailed in Section III-C.

Nozzle Switching. The Inkredible 3D bioprinter allows two different bioink cartridges to be used while printing the construct. An attack that disrupts the extracellular environment's cell patterns by switching the nozzles used during the construct's formation can alter cell-to-cell interactions and metabolic activity, ultimately affecting the construct's performance after transplantation into a patient. For demonstration and visual assessment, two different color dyes were used to distinguish between the hydrogels.

UV Attacks. A549 cells were embedded within gelatin-agarose hydrogel at $37°C$, and two ear shapes were printed at an extrusion pressure of approximately 30kPa. The constructs were exposed to 365nm wavelength UVA light during extrusion throughout the entire print duration. The UV doses, as reported by Cellink [56], were used for the calculations. Post-printing, the constructs were half-submerged in media, and were dyed with NucBlue (NB) Live Cell Stain and propidium iodide (PI) for cell viability analysis.

Thermodynamic Attacks. In this attack scenario, A549 cells were embedded within gelatin-agarose hydrogel at $37°C$, and two sets of squares were printed: one batch at a hydrogel temperature of $37°C$ and another at an increased temperature of $60°C$ to achieve noticeable effects on cell viability. Extrusion pressure was adjusted in each print scenario in order to obtain prints according to the established quality metrics. Post-printing, constructs were half-submerged in media and dyed with a NucBlue live cell stain kit and propidium iodide stain kit for cell viability analysis.

Z-Profile Attack. Cellink recommends a standoff distance equal to the nozzle's inner diameter [57] or 80% [58] of this height, depending on the material, a non-optimal standoff distance leads to a deformed print structure. Multiple three-layer square constructs ($8 * 8mm^2$) were printed, each with an added 0.5mm layer height. The sample control and attack prints were then used to calculate the impact of the attack on the Pr value.

QPIP. Two variations of QPIP were analyzed: the first on the outer geometry of a square construct and the second on the infill line of a shape construct. For the first attack, control
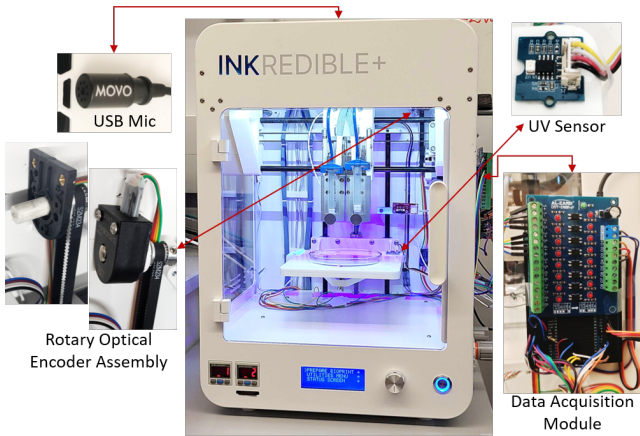
Fig. 4: BioSaFe Experimental Setup.

and attack samples were printed where a $2mm$ void was intentionally embedded by pausing the extrusion at all three layers in the sabotaged construct's lower-left corner. The prints were then used to calculate the attack's impact on the Pr value. In the second attack, an infill line was intentionally removed at the first layer of the ear print construct, which is obfuscated in the final build geometry.

Contamination Attack. In this attack the fan attached to the filtration unit is manipulated by sending in G-code command $M106$ with S_x parameter to adjust the fan speed. S_x specifies the speed on a scale from 0 to 255, where 255 corresponds to 100% fan speed.

B. BioSaFe Framework Implementation

The proposed framework is designed as a versatile implementation that can be easily integrated into existing EBB bioprinters, including the CELLINK INKREDIBLE+. The framework doesn't interfere with the regular printing operation, however, operator training is needed to use the alert interface. The printing setup includes a control PC connected through a USB interface with the printer. The control PC uses Cellink HeartWare software to slice the 3D geometry and serially transmit the G-code to the printer. The monitoring system (core i7, 16GB RAM, Linux OS) running the BioSafe is air-gapped from the printing environment.

1) Sensor Deployment: Table III provides a list of the sensors deployed on the bioprinter for monitoring various printing parameters. Factors such as accuracy, intrusivity, noise sensitivity, and calibration complexity were taken into account during the sensor selection process. Requiring minimal printer retrofitting and augmentation, the sensors do not interfere with regular operations once installed. Figure 4 illustrates the deployment of sensors on the INKREDIBLE+ 3D bioprinter and are detailed as follows;

- Optical rotary encoders were integrated with the x, y, and z-axes by adding extensions to the motor shafts. This involved attaching 8mm diameter cylinders to the shafts of each axis. While the coupling may introduce minor data errors due to slight misalignment, the algorithms in the framework efficiently compensate for these inaccuracies.

- For temperature measurement, surface adhesive thermistors were affixed to the metallic cartridge coupling, with one thermistor for each nozzle.
- To capture extrusion status, the signals were intercepted from the corresponding solenoid valves. These signals were then routed to an 8-channel optocoupler, which enables voltage level conversion (24V to 5V) and signal isolation.
- To measure UV intensity, a sensor was secured on the top of the print bed, positioned in a way that it does not interfere with nozzle movement.
- To capture HEPA filter fan status, a microphone was attached to the top of the printer near the fan.

These sensor deployments enable the collection of accurate data related to nozzle and bed positioning, extrusion status, nozzle temperature, UV intensity, and HEPA filter status while requiring minimal retrofitting for installation.

2) Data Acquisition Module: Data acquisition was performed using an Arduino-compatible Stemtera breadboard. This module not only captures real-time sensing data but also conducts data preprocessing before transmission. Interrupt-based programming was employed to capture encoder signals. The signal count per 1mm of linear movement along the x, y, and z axes was recorded. The count is then multiplied by the corresponding factor to accurately determine the nozzle (x/y-axis) and bed (z-axis) positions.

Analog pins were used to capture the nozzle temperature and UV intensity. For UV intensity, the analog-to-digital converter (ADC) was employed, and the value is mapped to three states: UV_{OFF}, UV_1 (365nm), and UV_2 (405nm). This mapping was achieved by recording the UV intensity at various distances between the UV source and the print bed and repeating it for both UV wavelengths. The analog value (T_a) from the temperature sensor was converted to the corresponding temperature reading using a simplified form of the Steinhart-Hart equation [59].

The sensing data collected from the physical domain is transmitted serially (baud rate 115200 bits/s) to the PC, where the cyber part of the BioSaFe framework operates. To ensure accurate monitoring, data related to parameters that change more frequently (x and y-axes) are updated at a higher sampling rate of $5ms$. On the other hand, data for parameters like the z-axis, temperature, and UV intensity, which exhibit less frequent changes or higher stability, is sampled at a lower rate of $50ms$. This approach reduces computation complexity on the PC while capturing essential information.

3) Data Transformation and Verification Module: The modules are implemented in Python 3 [60], leveraging several

Parameter	Sensing Type	Vendor	Unit Price (USD)	Model Number	Specs	Measurement Accuracy
x/y-axis	Optical Encoder	US Digital	100	E2-512-315-NE-H-D-B	512 cycles/rev	$\pm0.5mm$
z-axis	Optical Encoder	US Digital	100	E2-512-315-NE-H-D-B	512 cycles/rev	$\pm0.05mm$
Extrusion	Optocoupler	AL-ZARD	100	DST-1R8P-P	8 Channel	-
Nozzle Temperature	Thermister	Omega	80	SA1-TH-44006-40-T	$-80 \sim +120$ °C	±1°C
Fan Speed	Microphone	Movo	25	M1 USB	SNR 78dB Sen: -30dB	$\pm2\%$
UV status	UV Sensor	Grove	12	GUVA-S12D	Wavelength $200 \sim 370$nm	100%

TABLE III: Specification of deployed sensors.

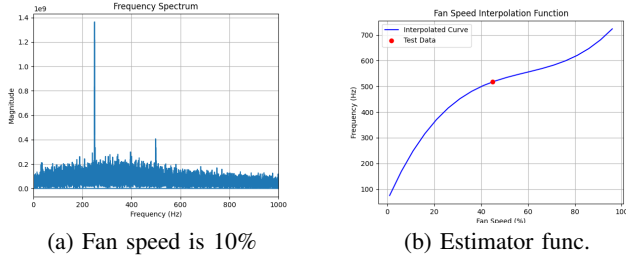(a) Fan speed is 10%   (b) Estimator func.

Fig. 5: Frequency spectrum and interpolation curve of the captured fan noise.

libraries for various tasks. For example, SciPy [61] is utilized for audio processing, Matplotlib [62] is employed for generating visualizations and plotting graphs, for image processing tasks, cv2 [63] is utilized, and pandas [64] is employed for data handling.

Besides transformation, the module is also responsible for periodically capturing the fan noise audio file. The audio samples of $5s$ duration are recorded every $5s$. The audio file is then subjected to FFT to convert to the frequency domain. The frequency spectrum for fan speed at 10% is shown in Figure 5a, wherein the peak corresponds to the fan noise. Multiple audio files with varying fan speeds are recorded to derive the estimation function. The maximum amplitude frequencies from these recordings are then measured and used as data points. A 3-degree polynomial is fitted to the data, as depicted in Figure 5b. This polynomial interpolation yields the estimator function for fan speed prediction. The calculation of fan speed is mathematically represented as follows;

$$fr_{spec} = fft(audio\_file.wav)$$

$$fr_p = max(|fr_{spec}|)$$

$$FS = f^3(fr_p)$$

The estimator function is subsequently tested on unknown data. For example, when tested on a 45% fan speed scenario, the estimator predicts the fan speed to be 46.5%.The recorded maximum deviation from the actual fan speed using the technique is within $\pm 2\%$.

4) Optimizing Thresholds: Thresholds specify the minimum deviations detectable by BioSaFe with current sensor settings. Using Gcode as a reference model, any deviations beyond these thresholds trigger an alert. The framework defines unique thresholds for different profiles to verify various printing processes accurately.This section highlights the maximum monitoring accuracy for different printing parameters, as setting thresholds below these limits may result in false +ves.

Geometry. The sensors in the x, and y-axes, due to mechanical coupling, add some noise to the data, thereby adding some dimensional inaccuracies to the sensor data layer representation. The image is passed through a 3*3 Gaussian and averaging filter to filter out these inaccuracies. The resultant difference image is subjected to a threshold of 110-pixel intensity to further remove noise. The filter size and the threshold value

are carefully chosen to remove maximum inaccuracies while retaining the required information.

Z-profile. The z-axis movement offers higher resolution (sensing accuracy: $\pm 10\mu m$) compared to the x,y axes. However, to raise alerts and detect sabotage, a threshold of $\pm 0.1mm$ is used for a single layer, and the accumulated z-profile threshold is limited not to exceed $\pm 0.2mm$. Deviations within this range are considered safe for benign bioprinting applications and do not trigger alerts.

Thermal profile. The temperature sensor used in the framework offers measurement accuracy of approximately $\pm 1\%$. Experimenting with the current bioprinting material has determined that the cell and shape integrity remain unaffected within a temperature range of $\pm 5\%$ of the intended temperature value. As a result, this range is adopted as the threshold for raising alerts, ensuring that any deviations within this range are considered safe and do not trigger unnecessary alarms.

Timing profile. Based on multiple experiments (Appendix D) the threshold is set to $\pm 1sec$ per layer and $\pm 2sec$ for the complete print. Any changes exceeding this threshold would generate an alert.

UV profile. Changing the intended UV source would generate an instant alert. However, for the duration and distance from the UV source, the thresholds are set to be $\pm 5s$ and $\pm 1mm$, respectively. Variations within these thresholds are considered safe for the print.

Fan speed profile. The current measurement accuracy for fan speed is within $\pm 2\%$ of the original value. A threshold of $> \pm 2\%$ is set for raising the alert.

VI. EVALUATION

This section details the results of the proposed attacks on printability and cell viability and evaluates the effectiveness of the proposed framework in detecting the attacks. Two types of constructs; a square and an ear shape are used for evaluation. The square shape, widely recognized as a standard tool for quality assurance, is employed to assess print parameters on bioink material and to evaluate attacks targeting the structural integrity of the construct, such as QPIP and Z-profile attacks. In contrast, an ear-shaped construct is used to demonstrate the framework's effectiveness in detecting attacks on complex geometries.

A. Evaluation of Sabotage Attacks

Nozzle Switching. The attack is evaluated on hydrogel using two different color dyes: transparent (Type 1) and orange (Type 2). The results from the attack are shown in Figures 6a and 6b. The attack leads to an evident change in the material composition, where the normal construct, originally intended to be printed with Type 1 hydrogel, now includes a layer of Type 2 hydrogel in between.
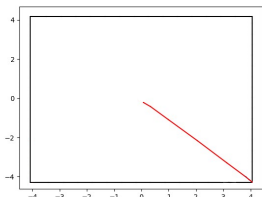
UV Attacks. Cell viability measured in control samples and UV attack samples did not produce conclusive results. This was due in part to the % viability directly after cell harvest being low before printing ($\sim 45\%$ on average) and cannot
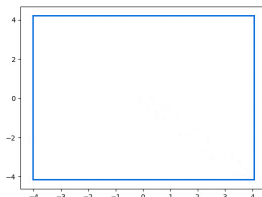
(a) Attack construct (top view)

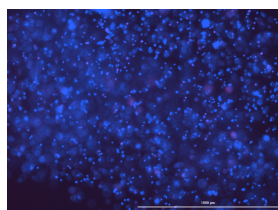(b) Attack construct (side view)

(c) Layer-1 of constuct
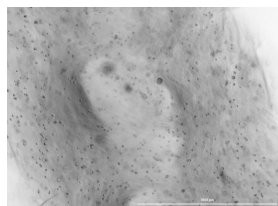
(d) Layer-2 of constuct

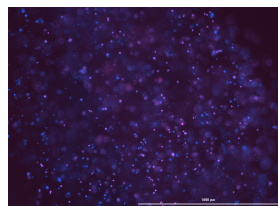Fig. 6: Nozzle Switching attack with spatiotemporal view.

(a) Control Construct

(b) Control Construct with NB and PI

(c) Attacked Construct

(d) Attacked Construct with NB and PI

Fig. 7: Cell viability after 24 hrs for normal and attacked construct

Day #	Print Construct	DAPI count (Total)	TR (Dead)	Live cells	% viability
Control	Construct 1	1153	34	1119	97
Day 0	Construct 2	589	8	581	98.6
Control	Construct 1	3235	402	2833	87.6
Day 1	Construct 2	3539	344	3195	90.3
Attack	Construct 1	2796	52	2744	98.1
Day 0	Construct 2	2533	37	2496	98.5
Attack	Construct 1	1997	562	1435	71.8
Day 1	Construct 2	2780	993	1787	64.3

TABLE IV: Cell viability of control (cells held at 37°C) and temperature attack (cells held at 60°C) print constructs.

Figure 7 presents the live/dead assay results for the print constructs taken at 24hrs (Day 1), as that is when the most comparison/contrast can be seen between the control and the attacked print. Blue indicates all cells and red/purplish-pink indicates dead cells. Figure 7b and 7d present the normal and attacked constructs with blue NB and red PI fluorescence overlaid, while Figure 7a and 7c represent the bright field images. Cell viability was measured at 0hrs (Day 0) and 24hrs (Day 1). For the control print, the average cell viability was found to be 97.8% at Day 0 and 88.9% at Day 1. In contrast, for the attacked prints, the cell viability was 98.3% at Day 0, but it significantly decreased to 68.1% at Day 1. The considerable decrease in cell viability in the attacked prints is attributed to the elevated temperature settings.

Z-profile Attack. Four squares were printed, with each increasing distance between the cartridge nozzle and the glass print bed. As the distance grew larger, print quality became more and more visually flawed, with unstable height measurements and Pr values, as shown in Figure 8. The Pr values of the attacks with an added z-magnitude of 0.5mm, 1.0mm, and 1.5mm were 0.93, 0.87, and 1.2 respectively. The Pr value for 1.5mm attack magnitude was found to be furthest from 1, indicating more deviation from the ideal square shape.

QPIP. Figure 9 illustrates the control and attacked samples along with the spatiotemporal view of the sensing data. The Pr value for the attacked construct was 0.85, while the normal print registered 0.92. The attack also significantly reduces the weight of the print constructs. Before printing, the mass of the glass print bed with a layer of 1% agarose solution was measured. After each print, the glass print bed was re-weighed. On average, individual control prints weighed 0.093g. Attacked prints weighed 0.052g. The pauses in print significantly decreased the total weight of the constructs by 43.7%. The $2mm$ void is easily visible in the print construct. A more concealed version of the attack is shown in Figure 11, wherein layer-1 of the ear geometry is compromised and is concealed in the final print geometry.

Contamination Attack. An ear construct was printed to assess the impact of bacterial contamination. The construct, printed with hydrogel but without embedded cells, was exposed to pathogens by turning off the HEPA filter. After incubating the construct for one week (at 37 °C), microscopic analysis revealed contamination. The results, shown in Figure 10, highlight bacterial colonies as dark spots in the print (Figure 10b),

be attributed to the 3D printing process. Post-print, the control cell viability remained relatively consistent ($\sim 41\%$ on average). On day 0 of the UV attack immediately post-print, cell viability reduced from $\sim 97\%$ viability before printing to $\sim 85\%$ viability post-print. The cell viability increased to $\sim 94\%$ on day 1, 24 hrs post-print, suggesting either cell recovery from UV damage and/or cell proliferation within the hydrogel. Despite cell recovery and proliferation, dead cells remain within the gel.

Thermodynamic Attacks. The results for the thermodynamic attacks are presented in Table IV, where, NB refers to the specific blue-fluorescent DNA stain used during fluorescence microscopy, and PI refers to the red-fluorescent DNA stain, both of which result in cells glowing blue or red under set wavelength filters. All raw cell viability counts were obtained using the BioTek Cytation 3 Cell Imaging Multi-Mode Reader.

Fig. 8: Z-profile attack on square construct.

(a) Control Construct   (b) Attacked Construct   (c) Attacked construct (layer-1)
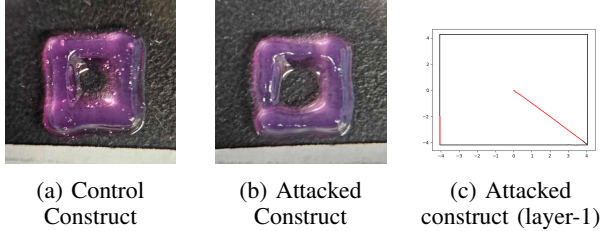
Fig. 9: QPIP attack on the 3-layer square construct.

(a) Normal Construct   (b) Contaminated Construct

Fig. 10: Contamination attack on ear construct, examined under a microscope with 3X zoom.

Sr. No.	Attacks	Verifying Profile	Attack Magnitude	Detection Performance	Detection type
1	Nozzle Switching	Geometry	$1mm$	Next layer	Visual
2	UV	UV Profile	UV type, $\Delta t > 1sec$ $\Delta z > 1mm$	Current layer	Alert
3	Nozzle Temp.	Thermal	$3°C$	$\Delta T > 2°C$	Alert
4	Layer Thickness	Z-Profile	$0.1mm$	Next layer	Alert
5	QPIP (Outer)	Geometry	$1mm$	Next layer	Visual
6	QPIP (Infill)	Geometry	$1mm$	Next layer	Visual
7	HEPA filter	Fan Speed	$\pm 2\%$	$5sec$	Alert
8	Print Speed	Timing	$\Delta S = 100mm/sec$	$\Delta t > 2sec$	Alert

TABLE V: BioSaFe attack detection performance.

while the uncontaminated print remained more translucent (Figure 10a).
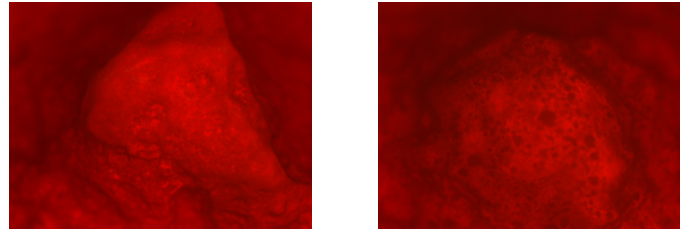
B. BioSaFe Evaluation

A total of 8 attack instances (6 proposed) were used to evaluate the proposed framework. The performance statistics are provided in Table V, and each profile evaluation is detailed in this section.

Extruder State. The BioSaFe framework monitors which nozzle is in the printing state and accordingly assigns the color black for nozzle 1 and blue for nozzle 2. The nozzle-switching attack was used to evaluate the framework's capability to detect any malicious extrusion state. This could, therefore, be easily detected by per-layer visual inspection of the print geometry. The spatiotemporal view of attacked construct layer-1 and layer-2 are shown in Figure 6c and 6d respectively. The anomaly could be identified once the sabotaged layer is printed and the spatiotemporal view is available.

UV Profile. BioSaFe validates the UV profile by monitoring the duration, standoff distance, and the UV type used for curing the print construct. The alert is triggered when the profile deviates from the original G-code instruction.

Thermal Profile. Depending on the material, the structural integrity starts to deteriorate at temperatures $> 2°C$ from the optimal print settings (see Appendix D). Also, the cell viability decreases at a higher ΔT. Since the framework with the measurement accuracy of $\pm 1°C$ takes time to stabilize, an alert is generated when ΔT exceeds the $2°C$ threshold and is reflected on the current or next print layer.

Z Profile. The optimal layer height as gathered through experimentation (see Appendix D) is $0.4mm$ and does not affect the Pr value with $\pm 0.05mm$ change in layer height. With the detection threshold of $\pm 0.1mm$ provided by BioSaFe for z-profile verification, the framework could detect changes after layer completion.

Geometry. BioSaFe monitors the extrusion status, along with other parameters; therefore, any changes that do not correspond with the G-code will be detected. Using per-layer visual representation, any pauses in extrusion (red lines) could easily be identified, as shown in Figure 11. The G-code and sensor data are compared using the geometry verification algorithm to generate a delta image after each print layer is completed. After applying filters and thresholding, the resultant delta image gives the exact location where the outer geometry/infill has been maliciously removed by the adversary.

HEPA Filter Profile. The detection accuracy provided by the framework is $\pm 2\%$. Conversely, the framework was evaluated for changes above the provided threshold and was able to validate the HEPA filter profile. Since BioSaFe records fan speed data every $5sec$, the detection performance is limited to a maximum of $5sec$.

Timing Profile. Print speed attacks were used to evaluate the timing profile. The optimal speed setting for the tested material is 600mm/sec (see Appendix D) with $\pm 100mm/sec$ variations that do not affect the Pr value. Using timing profile verification, the framework was able to detect the malicious changes when δt exceeds $2sec$. For the presented attack, the total print time for two benign constructs was 32 sec; however, with increased speed, the time was reduced to 27 sec.

VII. DISCUSSION AND LIMITATION

Table VI presents a comparative analysis of BioSaFe against current in-situ monitoring techniques. While much of the existing research focuses on fused deposition modeling (FDM) and monitors only a limited set of related printing parameters, none provide a comprehensive solution. Moreover, bioprinting introduces unique parameters that demand attention. The comparison underscores BioSaFe's capabilities in monitoring criti-
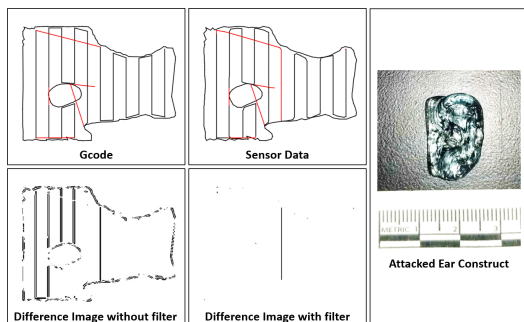
Fig. 11: Infill attack on human ear construct Layer 1.

Ref.	Printing Technique	Attack Magnitude							Detection Performance
		IF	OG	LT	UV	HF	Th	PS	
[21]	FDM	40%	-	-	-	-	-	-	0.98 AUC
[20]	FDM	0.25 mm	0.6 mm	-	-	-	-	-	4 False +ve/-ve
[31]	FDM	1%	1 mm	0.05 mm	-	-	5°C	2 sec	0 False +ve/-ve
[65]	FDM	-	10 mm	0.05 mm	-	-	-	-	94%
[30]	FDM	15%	-	0.1 mm	-	-	-	30 mm/sec	6% MAE
BioSaFe	EBB	1 mm	1 mm	0.1 mm	1 sec	± 2%	3°C	2 sec	0 False +ve/-ve

* IF: Infill, OG: Outer Geometry, LT: Layer Thickness, UV: Ultraviolet, HF: HEPA Filter, Th: Thermal, PS: Print Speed

TABLE VI: Performance comparison of BioSaFe against current in-situ monitoring techniques

Technology type	Bioink dispensing	BioSaFe monitored profiles						Potential sensing adaptations for BioSaFe
		Gm	LT	UV	HF	Th	PS	
Extrusion based [66]	Piston, Screw, Pneumatic	✓	✓	✓*	✓*	✓*	✓	Choose sensors based on extrusion type
Inkjet [67]	Piezoelectric, Thermal	✓	✓	-	✓*	✓*	✓	Integration of techniques to monitor the droplets
Laser induced [68]	Photothermal energy	✓	-	-	✓*	-	-	Laser parameters such as pulse width, duration, and frequency monitoring
Stereolitho-graphy [69]	Photothermal energy	✓	✓	✓	✓*	-	-	Calibrate UV sensors for different photopolymer sensitivities

* Gm: Geometry, LT: Layer Thickness, HF: HEPA Filter, Th: Thermal, PS: Print Speed

TABLE VII: BioSaFe scalability across other printing technologies

cal bioprinting parameters, while demonstrating its comparable detection performance with current state-of-the-art solutions.

The rest of the section details the security, scalability, and limitations of the BioSaFe framework.

A. Security against adaptive attacker

1) Exploiting detection thresholds: The thresholds are set by the framework based on the sensing accuracy. An adversary could learn these thresholds and attempt to go below the detection limits to sabotage print constructs. However, depending on the material properties, such small deviations might not affect the properties of the construct. Different bioink materials show different ranges of optimal printing settings. For a particular bioink, the methodology for finding these ranges is presented in Appendix D. For bioinks with optimal parameters that fall within the framework's threshold, current sensing may result in false negatives. To address this, the framework should be adapted by using sensors with precision matching the specific settings of the bioink material.

2) Multistage attacks: While the demonstrated attacks target individual print parameters, an adversary could manipulate multiple parameters to compromise the print construct. For example, an adversary could introduce subtle voids in the print geometry (QPIP) while altering the print temperature, reducing structural integrity and cell viability. BioSaFe with its modular nature and multifaceted profile verification could simultaneously check the integrity of individual print parameters and generate corresponding alerts.

3) Sampling attacks: An adversary could exploit the sensor sampling rate to evade detection. For instance, if the framework records readings at intervals of Δt, the adversary can introduce malicious changes between these samples. While

BioSaFe provides instantaneous and cumulative results for geometry, thickness, UV, and speed profiles, which can detect evasion attempts targeting the sampling rate, attackers can still exploit sampling limitations in thermal and fan speed profiles. For example, an attacker could avoid detection by manipulating fan speed between samples or exploiting delays in thermal readings. Reducing the sampling interval and using low-response-time sensors could help prevent such attacks.

B. Security against injection attacks

An adversary could attempt to attack the sensing equipment to disrupt the framework monitoring capabilities. For example, researchers have shown sensor readings could be manipulated through external electromagnetic interference [45]. However, employing proper shielding and implementing low-pass filters can help mitigate such interference.

C. BioSaFe framework scalability

The proposed monitoring framework is minimally intrusive, with little retrofitting required to add new sensors to an EBB printer. With no need for per-setup or per-geometry training requirements, the framework becomes more applicable in an industrial 4.0 environment with custom-designed specifications. Due to its layered architecture, BioSaFe can also be adapted to work with other bioprinting technologies. Table VII summarizes various technologies and outlines how BioSaFe could be integrated to monitor these processes. The symbol (✓*) indicates that the parameter may be involved but depends on the specific technology or post-processing.

D. Multilayer attacks

An attacker could manipulate print integrity by adding carefully crafted multilayer defects within threshold limits. In this scenario, the proposed per-layer analysis may not be enough to detect such adversarial changes. For instance, multiple geometry changes of $0.9mm$ across layers could compromise print integrity. Therefore, additional analysis is necessary, where sub-threshold defects are aggregated, possibly to the second layer. However, it is important to consider the strategic placement of these defects, as a simple aggregation approach could lead to an increase in false +ves.

VIII. CONCLUSION

Bioprinting enables the rapid fabrication of complex constructs and is being actively explored to assist in manufacturing human tissues, drug delivery systems, and cell-based

foods. Due to their use in critical nature applications, it is, therefore, necessary to secure such systems against adversarial attempts. This paper demoed practical sabotage attacks on the bioprinting process and used post-print quality assurance metrics such as printability and cell viability to ensure the impact of the attacks on bio constructs. It further presented an Industry 4.0-compliant BioSaFe defensive solution that supports mass customization while detecting sabotage attacks irrespective of construct geometry. BioSaFe can measure and analyze in-situ sensor data with G-code as a source of truth using spatiotemporal G-code modeling, enabling it by design to start monitoring from the first printing job. BioSaFe, given the material settings, was then successfully evaluated on our sabotage attacks and could accurately detect the anomalies for the given threshold.

REFERENCES

[1] C.-Y. Liaw and M. Guvendiren, "Current and emerging applications of 3d printing in medicine," *Biofabrication*, vol. 9, no. 2, p. 024102, 2017.

[2] Market. Us, "3D Bioprinting Market Data Analysis," *GlobeNewswire*, 2023.

[3] Y. S. Zhang, K. Yue, J. Aleman *et al.*, "3D Bioprinting for Tissue and Organ Fabrication," *Annals of biomedical engineering*, vol. 45, pp. 148–163, 2017.

[4] S. V. Murphy and A. Atala, "3d bioprinting of tissues and organs," *Nature biotechnology*, vol. 32, no. 8, pp. 773–785, 2014.

[5] S. Vijayavenkataraman, W.-C. Yan, W. F. Lu, C.-H. Wang, and J. Y. H. Fuh, "3d bioprinting of tissues and organs for regenerative medicine," *Advanced Drug Delivery Reviews*, vol. 132, pp. 296–332, 2018, 3D-Bioprinting and Micro-/Nano-Technology: Emerging Technologies in Biomedical Sciences.

[6] R. Augustine, S. N. Kalva, R. Ahmad, A. A. Zahid, S. Hasan, A. Nayeem, L. McClements, and A. Hasan, "3d bioprinted cancer models: Revolutionizing personalized cancer therapy," *Translational Oncology*, vol. 14, no. 4, p. 101015, 2021.

[7] B. A. de Melo, J. C. Benincasa, E. M. Cruz, J. T. Maricato, and M. A. Porcionatto, "3d culture models to study sars-cov-2 infectivity and antiviral candidates: From spheroids to bioprinting," *Biomedical Journal*, vol. 44, no. 1, pp. 31–42, 2021.

[8] S. Tian, H. Zhao, and N. Lewinski, "Key parameters and applications of extrusion-based bioprinting," *Bioprinting*, vol. 23, p. e00156, 2021.

[9] B. Webb and B. J. Doyle, "Parameter optimization for 3d bioprinting of hydrogels," *Bioprinting*, vol. 8, pp. 8–12, 2017.

[10] M. H. Rais, M. Ahsan, V. Sharma, R. Barua, R. Prins, and I. Ahmed, "Low-magnitude infill structure manipulation attacks on fused filament fabrication 3d printers," in *International Conference on Critical Infrastructure Protection*, 2022, pp. 205–232.

[11] M. Ahsan, M. H. Rais, and I. Ahmed, "Sok: Side channel monitoring for additive manufacturing - bridging cybersecurity and quality assurance communities," in *2023 IEEE 8th European Symposium on Security and Privacy (EuroS&P)*, 2023, pp. 1160–1178.

[12] T. Zandrini, S. Florczak, R. Levato, and A. Ovsianikov, "Breaking the resolution limits of 3d bioprinting: future opportunities and present challenges," *Trends in Biotechnology*, 2022.

[13] Z. Fu, V. Angeline, and W. Sun, "Evaluation of printing parameters on 3d extrusion printing of pluronic hydrogels and machine learning guided parameter recommendation," *International journal of bioprinting*, vol. 7, no. 4, 2021.

[14] G. Speit and P. Schütz, "Hyperthermia-induced genotoxic effects in human a549 cells," *Mutation Research/Fundamental and Molecular Mechanisms of Mutagenesis*, vol. 747, pp. 1–5, 2013.

[15] J. Shorrocks, N. D. Paul, and T. J. McMillan, "The dose rate of uva treatment influences the cellular response of hacat keratinocytes," *Journal of investigative dermatology*, vol. 128, no. 3, pp. 685–693, 2008.

[16] Y. Jin, W. Chai, and Y. Huang, "Printability study of hydrogel solution extrusion in nanoclay yield-stress bath during printing-then-gelation biofabrication," *Materials Science and Engineering: C*, vol. 80, pp. 313–325, 2017.

[17] D. Pamies, M. Leist, S. Coecke, G. Bowe, D. Allen, G. Gstraunthaler, R. de Vries, T. Hartung, and G. Stacey, "Guidance document on good cell and tissue culture practice 2.0 (gccp 2.0)," *ALTEX*, vol. 39, pp. 30–70, 2022.

[18] E. Kelly, "FDA regulation of 3D-printed organs and associated ethical challenges," *U. Pa. L. Rev.*, vol. 166, p. 515, 2017.

[19] J. M. Bliley, D. J. Shiwarski, and A. W. Feinberg, "3D-bioprinted human tissue and the path toward clinical translation," *Science Translational Medicine*, vol. 14, no. 666, p. eabo7047, 2022.

[20] Z. Yu, Y. Chang, S. Zhai, N. Deily, T. Ju, X. Wang, U. Jammalamadaka, and N. Zhang, "{XCheck}: Verifying integrity of 3d printed {Patient-Specific} devices via computing tomography," in *32nd USENIX Security Symposium (USENIX Security 23)*, 2023, pp. 2815–2832.

[21] C. Bayens, T. Le, L. Garcia, R. Beyah, M. Javanmard, and S. Zonouz, "See no evil, hear no evil, feel no evil, print no evil? malicious fill patterns detection in additive manufacturing," in *26th USENIX Security Symposium (USENIX Security 17)*, 2017, pp. 1181–1198.

[22] L. Graves, W. King, P. Carrion, S. Shao, N. Shamsaei, and M. Yampolskiy, "Sabotaging metal additive manufacturing: Powder delivery system manipulation and material-dependent effects," *Additive Manufacturing*, vol. 46, p. 102029, 2021. [Online]. Available: https://www.sciencedirect.com/science/article/pii/S2214860421001949

[23] S. Belikovetsky, Y. A. Solewicz, M. Yampolskiy, J. Toh, and Y. Elovici, "Digital audio signature for 3d printing integrity," *IEEE Transactions on Information Forensics and Security*, vol. 14, no. 5, pp. 1127–1141, 2018.

[24] S. R. Chhetri, A. Canedo, and M. A. Al Faruque, "Kcad: kinetic cyber-attack detection method for cyber-physical additive manufacturing systems," in *2016 IEEE/ACM International Conference on Computer-Aided Design (ICCAD)*. IEEE, 2016, pp. 1–8.

[25] J. Gatlin, S. Belikovetsky, S. B. Moore, Y. Solewicz, Y. Elovici, and M. Yampolskiy, "Detecting sabotage attacks in additive manufacturing using actuator power signatures," *IEEE Access*, vol. 7, pp. 133 421–133 432, 2019.

[26] M. Wu, H. Zhou, L. L. Lin, B. Silva, Z. Song, J. Cheung, and Y. Moon, "Detecting attacks in cybermanufacturing systems: Additive manufacturing example," in *MATEC Web of Conferences*, vol. 108. EDP Sciences, 2017, p. 06005.

[27] M. Wu, Z. Song, and Y. B. Moon, "Detecting cyber-physical attacks in cybermanufacturing systems with machine learning methods," *Journal of intelligent manufacturing*, vol. 30, pp. 1111–1123, 2019.

[28] A. Al Mamun, C. Liu, C. Kan, and W. Tian, "Securing cyber-physical additive manufacturing systems by in-situ process authentication using streamline video analysis," *Journal of Manufacturing Systems*, vol. 62, pp. 429–440, 2022.

[29] ——, "Real-time process authentication for additive manufacturing processes based on in-situ video analysis," *Procedia Manufacturing*, vol. 53, pp. 697–704, 2021.

[30] Y. Gao, B. Li, W. Wang, W. Xu, C. Zhou, and Z. Jin, "Watching and safeguarding your 3d printer: Online process monitoring against cyber-physical attacks," *Proceedings of the ACM on Interactive, Mobile, Wearable and Ubiquitous Technologies*, vol. 2, no. 3, pp. 1–27, 2018.

[31] M. H. Rais, Y. Li, and I. Ahmed, "Spatiotemporal g-code modeling for secure fdm-based 3d printing," in *Proceedings of the ACM/IEEE 12th International Conference on Cyber-Physical Systems*, 2021, pp. 177–186.

[32] A. Slaughter, M. Yampolskiy, M. Matthews, W. E. King, G. Guss, and Y. Elovici, "How to Ensure Bad Quality in Metal Additive Manufacturing: In-Situ Infrared Thermography from the Security Perspective," in *Proceedings of the 12th International Conference on Availability, Reliability and Security*, ser. ARES '17. New York, NY, USA: Association for Computing Machinery, 2017. [Online]. Available: https://doi.org/10.1145/3098954.3107011

[33] A. Chabot, N. Laroche, E. Carcreff, M. Rauch, and J.-Y. Hascoët, "Towards defect monitoring for metallic additive manufacturing components using phased array ultrasonic testing," *Journal of Intelligent Manufacturing*, vol. 31, no. 5, pp. 1191–1201, 2020.

[34] M. H. Rais, Y. Li, and I. Ahmed, "Dynamic-thermal and localized filament-kinetic attacks on fused filament fabrication based 3d printing process," *Additive Manufacturing*, vol. 46, p. 102200, 2021. [Online]. Available: https://www.sciencedirect.com/science/article/pii/S2214860421003614

[35] J. C. Isichei, S. Khorsandroo, and S. Desai, "Cybersecurity and privacy in smart bioprinting," *Bioprinting*, p. e00321, 2023.

[36] C. Xiao, "Security attack to 3d printing," *xFocus Information Security Conference*, 2013.

[37] S. B. Moore, W. B. Glisson, and M. Yampolskiy, "Implications of malicious 3d printer firmware," in *Proceedings of the 50th Hawaii International Conference on System Sciences*, 2017.

[38] H. Pearce, K. Yanamandra, N. Gupta, and R. Karri, "Flaw3d: A trojan-based cyber attack on the physical outcomes of additive manufacturing," *IEEE/ASME Transactions on Mechatronics*, 2022.

[39] E. Kurkowski, A. Van Stockum, J. Dawson, C. Taylor, T. Schulz, and S. Shenoi, "Manipulation of g-code toolpath files in 3d printers: Attacks and mitigations," in *International Conference on Critical Infrastructure Protection*. Springer, 2022, pp. 155–174.

[40] M. McCormack, S. Chandrasekaran, T. Yu, S. Wolf, and V. Sekar, "C3po: A security analysis tool for networked 3d printers (cmu-cylab-19-002)."

[41] L. D. Sturm, C. B. Williams, J. A. Camelio, J. White, and R. Parker, "Cyber-physical vulnerabilities in additive manufacturing systems," in *2014 International Solid Freeform Fabrication Symposium*. University of Texas at Austin, 2014.

[42] S. Belikovetsky, M. Yampolskiy, J. Toh, J. Gatlin, and Y. Elovici, "dr0wned–{Cyber-Physical} attack with additive manufacturing," in *11th USENIX Workshop on Offensive Technologies (WOOT 17)*, 2017.

[43] A. Van Stockum, E. Kurkowski, T. Potok, C. Taylor, J. Dawson, M. Rice, and S. Shenoi, "Attack-defense modeling of material extrusion additive manufacturing systems," in *International Conference on Critical Infrastructure Protection*. Springer, 2022, pp. 121–153.

[44] S. Moore, P. Armstrong, T. McDonald, and M. Yampolskiy, "Vulnerability analysis of desktop 3d printer software," in *2016 Resilience Week (RWS)*, 2016, pp. 46–51.

[45] Y. Tu, S. Rampazzi, B. Hao, A. Rodriguez, K. Fu, and X. Hei, "Trick or heat? manipulating critical temperature-based control systems using rectification attacks," ser. CCS '19. New York, NY, USA: Association for Computing Machinery, 2019, p. 2301–2315. [Online]. Available: https://doi.org/10.1145/3319535.3354195

[46] D. Kushner, "The real story of stuxnet," *ieee Spectrum*, vol. 50, no. 3, pp. 48–53, 2013.

[47] L. Goers, P. Freemont, and K. M. Polizzi, "Co-culture systems and technologies: taking synthetic biology to the next level," *Journal of The Royal Society Interface*, vol. 11, no. 96, p. 20140065, 2014.

[48] M. Kciuk, B. Marciniak, M. Mojzych, and R. Kontek, "Focus on uv-induced dna damage and repair—disease relevance and protective strategies," *International Journal of Molecular Sciences*, vol. 21, no. 19, p. 7264, 2020.

[49] M. Klak, M. Gomółka, T. Dobrzański, G. Tymicki, P. Cywoniuk, P. Kowalska, K. Kosowska, T. Bryniarski, A. Berman, A. Dobrzyń *et al.*, "Irradiation with 365 nm and 405 nm wavelength shows differences in dna damage of swine pancreatic islets," *PLoS One*, vol. 15, no. 6, p. e0235052, 2020.

[50] V. H. Mouser, F. P. Melchels, J. Visser, W. J. Dhert, D. Gawlitta, and J. Malda, "Yield stress determines bioprintability of hydrogels based on gelatin-methacryloyl and gellan gum for cartilage bioprinting," *Biofabrication*, vol. 8, no. 3, p. 035003, 2016.

[51] L. Ouyang, R. Yao, S. Mao, X. Chen, J. Na, and W. Sun, "Three-dimensional bioprinting of embryonic stem cells directs highly uniform embryoid body formation," *Biofabrication*, vol. 7, no. 4, p. 044101, 2015.

[52] M. Alruwaili, J. A. Lopez, K. McCarthy, E. G. Reynaud, and B. J. Rodriguez, "Liquid-phase 3d bioprinting of gelatin alginate hydrogels: influence of printing parameters on hydrogel line width and layer height," *Bio-Design and Manufacturing*, vol. 2, pp. 172–180, 2019.

[53] Z. Fu, S. Naghieh, C. Xu, C. Wang, W. Sun, and X. Chen, "Printability in extrusion bioprinting," *Biofabrication*, vol. 13, no. 3, p. 033001, 2021.

[54] F. Scocozza, M. Sakaj, F. Auricchio, S. Marconi, P. Riello, C. Ferrari, L. Cansolino, L. Catenacci, M. Sorrenti, M. Scatto *et al.*, "Shape fidelity and sterility assessment of 3d printed polycaprolactone and hydroxyapatite scaffolds," *Journal of Polymer Research*, vol. 28, pp. 1–13, 2021.

[55] CELLINK, "CELLINK INKREDIBLE + brochure," Latest Accessed: May, 2024. [Online]. Available: https://www.cellink.com/wp-content/uploads/2022/03/INKREDIBLE-16P_Digital-3.pdf

[56] ——, "GelMA Crosslinking Recommendations ," 2018, Latest Accessed: May, 2024. [Online]. Available: https://www.cellink.com/wp-content/uploads/2018/04/GelMA_crosslinking_protocol.pdf

[57] ——, "CELLINK Support," 2018, Latest Accessed: May, 2024. [Online]. Available: https://www.cellink.com/wp-content/uploads/2018/04/CELLINKSupportApplicationNote.pdf

[58] ——, "CELLINK Printing Protocol," 2023, Latest Accessed: May, 2024. [Online]. Available: https://www.cellink.com/wp-content/uploads/2023/02/Printing-Protocol-PCL_2-Jan-2023.pdf

[59] J. S. Steinhart and S. R. Hart, "Calibration curves for thermistors," in *Deep sea research and oceanographic abstracts*, vol. 15, no. 4. Elsevier, 1968, pp. 497–503.

[60] Python Software Foundation, "Python 3.11.4 documentation," 2024. [Online]. Available: https://docs.python.org/3/

[61] SciPy development team, "SciPy documentation," 2024. [Online]. Available: https://docs.scipy.org/doc/scipy/

[62] Matplotlib development team, "Matplotlib 3.9.0 documentation," 2024. [Online]. Available: https://matplotlib.org/stable/index.html

[63] OpenCV Team, "opencv-python 4.8.0.74," 2023. [Online]. Available: https://pypi.org/project/opencv-python/

[64] pandas development team, "Pandas documentation," 2024. [Online]. Available: https://pandas.pydata.org/docs/

[65] H. Zhou, C. Liu, W. Tian, and C. Kan, "Echo state network learning for the detection of cyber attacks in additive manufacturing," in *2021 IEEE 17th International Conference on Automation Science and Engineering (CASE)*, 2021, pp. 177–182.

[66] Y. S. Zhang, G. Haghiashtiani, T. Hübscher, D. J. Kelly, J. M. Lee, M. Lutolf, M. C. McAlpine, W. Y. Yeong, M. Zenobi-Wong, and J. Malda, "3d extrusion bioprinting," *Nature Reviews Methods Primers*, vol. 1, no. 1, p. 75, 2021.

[67] X. Li, B. Liu, B. Pei, J. Chen, D. Zhou, J. Peng, X. Zhang, W. Jia, and T. Xu, "Inkjet bioprinting of biomaterials," *Chemical Reviews*, vol. 120, no. 19, pp. 10 793–10 833, 2020.

[68] M. Ali, E. Pages, A. Ducom, A. Fontaine, and F. Guillemot, "Controlling laser-induced jet formation for bioprinting mesenchymal stem cells with high viability and high resolution," *Biofabrication*, vol. 6, no. 4, p. 045001, 2014.

[69] H. Kumar and K. Kim, "Stereolithography 3d bioprinting," *3D bioprinting: principles and protocols*, pp. 93–108, 2020.

[70] A. Dravid, A. McCaughey-Chapman, B. Raos, S. J. O'Carroll, B. Connor, and D. Svirskis, "Development of agarose–gelatin bioinks for extrusion-based bioprinting and cell encapsulation," *Biomedical Materials*, vol. 17, no. 5, p. 055001, 2022.

APPENDIX

A. Data Representation

1) Space Domain Representation: The 3D layer map (LM) of the print geometry could be represented as a set of 2D layers (LY_k), with each layer start and end mapped to the layer change events.

$$LM = \begin{bmatrix} LY_1 \\ LY_2 \\ .. \\ LY_m \end{bmatrix} \text{ where m = number of layers} \qquad (3)$$

where each layer is represented as a set of point attributes (PA_{x_k,y_k}). Each point in this layer representation could be presented as a tuple of printer attributes, including nozzle positions in the x (NP_x) and y-axis (NP_y), and extrusion state (ES_i).

$$PA_{x_k,y_k} = (NP_x, NP_y, ES_i) \qquad (4)$$

The 2D layer map LY_k could, therefore, be represented as a 2D array as shown in equation 5.

$$LY_k = \begin{bmatrix} PA_{1,1} & PA_{1,2} & ... & PA_{1,j} \\ PA_{2,1} & PA_{2,2} & ... & PA_{2,j} \\ . & . & ... & . \\ PA_{1,1} & PA_{1,2} & ... & PA_{1,j} \\ PA_{i,1} & PA_{i,2} & ... & PA_{i,j} \end{bmatrix} \qquad (5)$$

The layer change events (LC) marking the end and beginning of each layer map are represented as a uni-directional array of z-axis displacement (z_k), between the nozzle and the print bed, as shown in equation 6.

$$LC = [z_1, z_2, ..., z_k, ..., z_m] \tag{6}$$

The space domain representation matrix of the 3D geometry could, therefore, be represented as a matrix containing a tuple of z-axis displacement (z_k) and per layer map (LY_k) as shown in equation 7.

$$SDR_{3D} = [(z_1, LY_1), (z_2, LY_2), ..., (z_k, LY_k), ..., \\ (z_m, LY_m)] \tag{7}$$

Printing parameters, including nozzle temperature (NT_i), UV curing (UV_i), and fan speed (FS) in the space domain, do not provide any additional advantage in data analysis and, therefore, are not represented in the format.

2) Time Domain Representation: For the time series representation of data, just like in the space domain, the layer change event is taken as boundary conditions to determine per layer time sampled data (TP_k) as shown in equation 8:

$$TP_k = [(t_1, PS_1), (t_2, PS_2), ..., (t_n, PS_n)] \tag{8}$$

where printer state, (PS_k), includes attributes like nozzle position, nozzle temperature, extrusion state, UV state, and the fan speed, represented as $PS_k = (NP_x, NP_y, NT_i, ES_i, UV_i, FS)$. In the time domain, a 3D geometry is expressed by a uni-dimensional array containing tuples of z-axis information (z_k) and per layer time sampled data (TP_k) as shown in equation 9.

$$TDR_{3D} = [(z_1, TP_1), (z_2, TP_2), ..., (z_k, TP_k), ..., \\ (z_m, TP_m)] \tag{9}$$

B. Algorithms

Given the initial and final end points along maximum speed and acceleration Algortihm 1 outputs time series array containing nozzle position at each ΔT time interval. Algorithm 2 converts G-code to spacial representation and outputs a per layer plot.

Algorithm 1 Time Domain Transformation Function

Input: $NP_{x1}, NP_{y1}, NP_{x2}, NP_{y2}, v_{max}, a_{max}$

  $x_1 \leftarrow NP_{x1}, x_2 \leftarrow NP_{x2}, y_1 \leftarrow NP_{y1}, y_2 \leftarrow NP_{y2}$
  $D \leftarrow \sqrt{(x_2 - x_1)^2 - (y_2 - y_1)^2}$
  $\theta \leftarrow tan^{-1}((y_2 - y_1)/(x_2 - x_1))$
  $S \leftarrow \sqrt{D * a_{max}}$
  if $S < v_{max}$ **then**   ▷ Triangular motion
    $T \leftarrow 2\sqrt{D/a_{max}}$
    $t \leftarrow T/2, d \leftarrow a_{max}t^2/2$
    while $temp < T$ **do**
      $t_i \leftarrow temp * \Delta t$
      if $temp < t_i$ **then**   ▷ Acceleration phase
        $\Delta d \leftarrow 0.5 * a_{max} * t_i^2$
      else   ▷ Deceleration phase
        $\Delta d \leftarrow d + S * t_i - 0.5 * a_{max} * t_i^2$
      end if
      $intp\_x \leftarrow \Delta d cos\theta$
      $intp\_y \leftarrow \Delta d |sin\theta|$
      $TSD\_array \leftarrow insert(t_i, intp\_x, intp\_y)$
    end while
  end if
  return TSD_array

Algorithm 2 Space Domain Transformation Function

Input: $NP_{x1}, NP_{y1}, NP_{x2}, NP_{y2}, ES$
Output: plot_{layerNum}.png

  $x_1 \leftarrow NP_{x1}, x_2 \leftarrow NP_{x2}, y_1 \leftarrow NP_{y1}, y_2 \leftarrow NP_{y2}$
  Open new Plot
  if ES_1 is high **then**   ▷ Nozzle 1 is active
    $Color \leftarrow$ **black**
    Plot black-line using the coordinates
  else if ES_2 is high **then**   ▷ Nozzle 2 is active
    $Color \leftarrow$ **blue**
    Plot blue-line using the coordinates
  else
    $Color \leftarrow$ **red**   ▷ No extrusion
    Plot red-line using the coordinates
  end if
  if $LC_i == TRUE$ **then**   ▷ Layer change event
    Save **plot_{layerNum}.png**
    Close current plot
    Open a new plot
  end if

C. Bioink Preparation

After testing a number of different hydrogel formulations, the gelatin-agarose gel was chosen due to gel strength, short preparation time, and the non-compulsion of a chemical crosslinking step. A polymer concentration of 2% gelatin / 2% agarose weight per volume was used due to its smaller swelling ratio [70].

To prepare the gelatin-agarose gel, 0.2g of gelatin (Type-A) was mixed with 5 mL of DMEM cell media in a glass vial to make the gelatin solution. Then, 0.2g of agarose was mixed

with 5mL of DMEM cell media in a glass vial to make the agarose solution. The gelatin solution was placed on a hotplate at 55°C with a magnetic stir bar stirring at 1000 rpm for 1 hr. While the gelatin solution was stirred, the agarose solution was placed on a hotplate with a magnetic stir bar at 1000 rpm and allowed to reach 80°C. After about 10 mins, when the solution reached 80°C and appeared to be clear, the temperature was gradually dropped to $\geq$65°C. In a warm 50mL beaker, both solutions were mixed on a hotplate at 55°C and 1000 rpm for 10 mins. For thermodynamic and UV attacks for the evaluation of cell viability, A549 cells were embedded in the hydrogel at a concentration of 3 million cells per mL of hydrogel and printed immediately.

D. Finding optimal bioink settings

For finding the optimal printing parameters for the bioink, we used the printability ratio (Pr) and printability optimization index (POI) values [9]. POI is a dimensionless ratio that uses nozzle diameter, extrusion pressure, and filament width to determine how well a geometry can be printed with higher accuracy and lower extrusion pressure. The higher the POI, the higher the accuracy and quality of print that can be made with a lower extrusion pressure. The purpose of this parameter is to find the best way to minimize shear stress when printing the cells. Mathematically Pr and POI are defined as follows;

$$Pr = L^2/16A$$

$$POI = 1/W_a * E_p * N_d$$

Where L is the parameter, A is the area, W_a is the average width, E_p is the extrusion pressure, and N_d is the nozzle inner diameter. The printing settings were optimized based on the Pr and POI values plus the number of well-constructed prints (not broken).

Square constructs were printed at different temperatures, speeds, and layer height settings to find the effects of increasing them on the Pr and POI values. 2%/2% Agarose-Gelatin in 10 mL of Complete Media (Complete DMEM) was used for experimentation. Each construct was repeated 3 times, and the average was calculated to get more consistent results.

Temperature Settings:. For the temperature, the results are presented in Table VIII. The constructs were printed with a step of 3°C starting at 37°C. Below 37°C, the bioink starts to coagulate and doesn't extrude properly. The optimal Pr and POI values were found to be 0.924 and 0.291 at 37°C. For temperature ranges tested, there were no broken prints; however, at higher temperatures (> 49°C), the construct starts to coalesce as shown in Figure 12.

Speed Settings:. For the speed, the results are presented in Table IX. The constructs were printed with a step of $50mm/s$ starting at $500mm/s$. The optimal Pr and POI values were found to be between the range of $550-600mm/s$. At higher speeds the construct starts to break, as shown in Figure 13.

Layer Height:. For the layer height, the results are presented in Table X. The constructs were printed with a step of $0.5mm$, staring at a distance of $0.5mm$. The optimal Pr and POI values were found to be 0.998 and 0.274 at $0.5mm$ layer height. The construct starts to break at a higher nozzle distance, as shown in Figure 14.
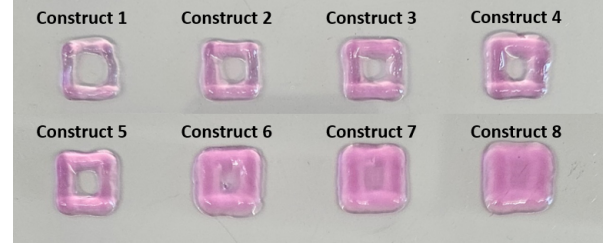

Fig. 12: Square print construct at different ranges of temperature values.
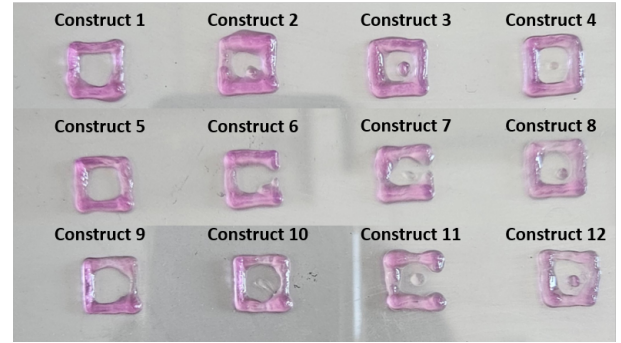

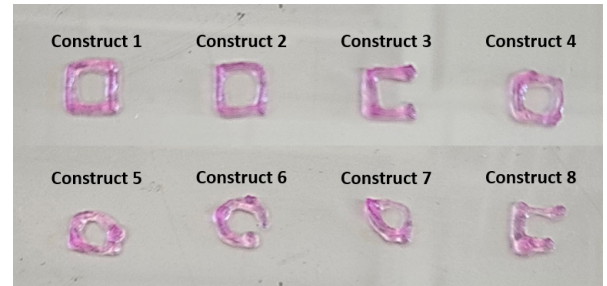Fig. 13: Square print construct at different ranges of speed values.

Fig. 14: Square print construct at different ranges of layer height values.

	$Temp$ $C°$	$W1_{avg}$ (mm)	$W2_{avg}$ (mm)	$W3_{avg}$ (mm)	$W4_{avg}$ (mm)	W_a (mm)	L (mm)	A (mm²)	Pr	POI
Construct 1	37	0.268	0.295	0.235	0.245	0.261	1.898	0.255	0.924	0.291
Construct 2	40	0.324	0.337	0.235	0.276	0.293	1.586	0.189	0.838	0.259
Construct 3	43	0.350	0.424	0.364	0.303	0.360	1.131	0.099	0.840	0.212
Construct 4	46	0.360	0.419	0.452	0.441	0.418	0.862	0.056	0.848	0.181
Construct 5	49	0.336	0.365	0.382	0.359	0.361	1.259	0.117	0.847	0.210

Pressure (E_p): 32kPa, Nozzle Inner Dia. (N_d): 0.413mm

TABLE VIII: Pr and POI values at different temperature ranges.

	$Speed$ mm/s	Broken Constructs	$W1_{avg}$ (mm)	$W2_{avg}$ (mm)	$W3_{avg}$ (mm)	$W4_{avg}$ (mm)	W_a (mm)	L (mm)	A (mm²)	Pr	POI
Construct 1	500	0	0.250	0.296	0.200	0.239	0.246	1.789	0.239	0.844	0.309
Construct 2	550	0	0.284	0.242	0.285	0.236	0.262	1.671	0.192	0.929	0.299
Construct 3	600	0	0.217	0.231	0.230	0.260	0.235	1.985	0.222	1.130	0.334
Construct 4	650	2	0.200	0.215	0.214	0.207	0.209	2.099	0.325	0.847	0.362
Construct 5	700	1	0.203	0.204	0.183	0.235	0.206	2.098	0.333	0.827	0.371
Construct 6	750	2	0.238	0.209	0.255	0.259	0.240	1.993	0.297	0.836	0.315
Construct 7	800	2	0.273	0.296	0.255	0.214	0.260	1.682	0.210	0.842	0.292
Construct 8	850	1	0.152	0.162	0.217	0.246	0.194	2.058	0.321	0.834	0.393
Construct 9	900	1	0.199	0.164	0.202	0.149	0.178	2.120	0.333	0.845	0.425
Construct 10	950	2	0.140	0.127	0.145	0.211	0.156	2.039	0.308	0.844	0.486
Construct 11	1000	3	-	-	-	-	-	-	-	-	-
Construct 12	1050	2	0.140	0.209	0.185	0.276	0.203	1.912	0.265	0.862	0.374

Pressure (E_p): 32kPa, Nozzle Inner Dia. (N_d): 0.413mm

TABLE IX: Pr and POI values at different speed ranges.

	LH (mm)	Broken Constructs	$W1_{avg}$ (mm)	$W2_{avg}$ (mm)	$W3_{avg}$ (mm)	$W4_{avg}$ (mm)	W_a (mm)	L (mm)	A (mm²)	Pr	POI
Construct 1	0.5	0	0.313	0.313	0.26	0.217	0.275	1.648	0.17	0.998	0.274
Construct 2	1	0	0.13	0.148	0.15	0.147	0.144	2.2	0.326	0.928	0.526
Construct 3	1.5	1	0.25	0.23	0.2	0.22	0.225	1.89	0.25	0.893	0.336
Construct 4	2	1	0.185	0.164	0.149	0.212	0.178	1.788	0.237	0.843	0.426
Construct 5	2.5	2	0.178	0.321	0.135	0.232	0.217	1.628	0.193	0.858	0.349
Construct 6	3	2	0.16	0.144	0.221	0.218	0.186	1.195	0.108	0.826	0.407

Pressure (E_p): 32kPa, Nozzle Inner Dia. (N_d): 0.413mm

TABLE X: Pr and POI values at different layer height ranges.